Decoding Cathode-Electrolyte Interface Issues in Conventional Ethers Electrolytes-Based Magnesium Rechargeable Batteries

*Ruijie Zhu, Takashi Yabu, Cheng Yang, Huijun Yang, Akira Nasu, Toshihiko Mandai, Masaki Matsui, and Hiroaki Kobayashi**

Dr. R. Zhu, T. Yabu, Dr. A. Nasu, Prof. M. Matsui, Dr. H. Kobayashi
Department of Chemistry, Faculty of Science, Hokkaido University
Sapporo 060-0810, Japan
E-mail: h.kobayashi@sci.hokudai.ac.jp

C. Yang
Institute for Catalysis, Hokkaido University
Sapporo 001-0021, Japan

H. Yang
Department of Chemical System Engineering, The University of Tokyo
Tokyo 113-8656, Japan.

T. Mandai
Research Center for Energy and Environmental Materials, National Institute for Materials Science (NIMS)
Tsukuba 305-0044, Japan

Keywords: magnesium rechargeable batteries, current collector corrosion, weakly coordinating anion, trace water, electrolyte decomposition

Magnesium rechargeable batteries (MRBs), as a promising candidate for next-generation high-energy batteries, offer inherent advantages in terms of resource availability and safety. To identify the key factors for achieving high-voltage MRBs, this study investigates ether-based weakly coordinating anion (WCA) electrolytes—$Mg[B(OCH(CF_3)_2)_4]_2$ (BHFIP) and $Mg[Al(OCH(CF_3)_2)_4]_2$ (AlHFIP)—under varying water content to elucidate their electrochemical behavior on carbon-coated Al current collectors and MnO_2 cathodes. The two electrolytes are found to exhibit different characteristics in moisture, but as a common conclusion, trace water can promote electrolyte decomposition and CEI formation. Ultimately, the BHFIP electrolyte designed with a low water content successfully enables reversible $Mg||MnO_2$ cells cycling under high voltage (4 V cut-off, > 50 cycles) by mitigating side reactions, whereas higher water content accelerates solvent/anion decomposition and MnO_2 dissolution. The work highlights trace water content as a critical factor in ether-based MRB's electrolyte design, demonstrating that optimized BHFIP electrolytes have potential in stabilizing high-voltage MRBs while emphasizing the need for moisture-resistant functional materials to enhance battery performance.

1. Introduction

With the rise of concepts such as electric vertical take-off and landing (eVTOL) and electric shipping,[1] the demand for high-energy-density batteries has become a prominent call in the post-lithium-ion battery era. Magnesium rechargeable batteries (MRBs) that directly use magnesium (Mg) metal as the anode are gaining increasing attention due to the high capacity of Mg anodes (3833 mAh cm^{-3}), its natural abundance, better air stability compared to alkali metals, and enhanced safety.[2] Currently, mainstream MRB electrolytes can be categorized into two main types. The first type, introduced by Aurbach et al., is based on Grignard reagents,[3] such as all phenyl complex (APC) electrolytes.[4] The second type involves conventional Mg salts dissolved in ether-based solvents, such as magnesium bis(trifluoromethanesulfonyl)imide ($Mg(TFSI)_2$) dissolved in dimethoxyethane (DME) or tetrahydrofuran (THF) to form an electrolyte, and further incorporating additives containing halide ions to enhance the reversibility of Mg deposition.[5] In recent years, a novel class of ether-based weakly coordinating anions (WCA) electrolytes,[6] such as magnesium tetrakis(hexafluoroisopropyloxy)borate ($Mg[B(hfip)_4]_2$), has been developed.[7] These electrolytes enable reversible Mg metal deposition with high coulombic efficiency and exhibit an electrochemical stability window typically no less than 3.5 V. Compared to Grignard reagent-based electrolytes, the preparation of $Mg[B(hfip)_4]_2$ electrolytes is simpler, with enhanced safety and significantly reduced sensitivity to humidity. It is also a halogen-free electrolyte, which solves the problem of corrosion of electrodes by halogen ions.[8] These advantages endow the $Mg[B(hfip)_4]_2$ based electrolytes with substantial potential for practical applications in MRBs. However, the understanding of ether-based electrolytes with $Mg[B(hfip)_4]_2$ (or similar magnesium salts) remains incomplete, with significant discrepancies in test data across different laboratories—an issue commonly observed in MRB research. The specific electrochemical characteristics of such electrolytes are still a subject of considerable debate. On the other hand, the stability of $Mg[B(hfip)_4]_2$ electrolytes at high voltage has made

it possible to explore the use of high-voltage materials in MRBs. Low-cost transition metal oxides (TMOs), such as manganese dioxide (MnO_2), are known for their theoretically high energy density and have been demonstrated to reversibly store Mg ions.[9] However, due to the small ionic radius and high charge density of Mg ions, their insertion and extraction in conventional TMOs are challenging. [10] The sluggish ion diffusion leads to high overvoltage, and most of the TMOs cathode materials show some catalytic activity,[11] which further aggravates the decomposition of the electrolyte at high voltage, which results in incomplete charging and severe side reactions caused by high overpotential, limiting the study of Mg storage mechanisms in these materials.[12] Understanding the electrochemical characteristics of this electrolyte system at high voltages, as well as the changes in the electrolyte-electrode interface within MRBs, is crucial for developing high-energy-density MRBs and advancing the material design strategy for MRBs.

Therefore, in this work, we compared the electrochemical stability of tetrakis(hexafluoroisopropyloxy) aluminate ($Mg[Al(hfip)_4]_2$) based electrolytes and $Mg[B(hfip)_4]_2$ based electrolytes on carbon-coated aluminum (Al) foil (used as the cathode current collector) under high voltage conditions. By preparing electrolytes with varying water content, we observed that $Mg[B(hfip)_4]_2$ and $Mg[Al(hfip)_4]_2$ exhibit entirely different behaviors in H_2O-contained environments. Furthermore, we confirmed that trace amounts of water in these electrolytes not only affect the performance of the Mg metal anode but also influence the cycling stability of the battery by promoting electrolyte decomposition and electrode material dissolution. This indicates that these WCA electrolytes may not be as resistant to water as previously reported.[13] However, by controlling the H_2O content to low levels acceptable in industrial production (e.g. $\leq$ 200ppm), Mg||MnO_2 batteries can achieve reversible charge and discharge at relatively high cut-off voltages (4 V). This provides critical insights into the development of high-performance electrolytes and electrode materials for MRBs, and may provide further reference for other ion batteries that utilize similar electrolyte systems.[14]

2. Results and Discussion

Our curiosity is about the electrochemical behavior of WCA-based electrolytes on the cathode side from our exploration of high-energy-density Mg||MnO_2 batteries. As shown in **Figure 1(a)**, using an electrolyte formed by dissolving $Mg[B(hfip)_4]_2$ salt in diethylene glycol dimethyl ether (DEGDME, G2) as an example, the anion, trace amounts of water, and solvents (including DEGDME and DME, since the crystallized form of the $Mg[B(hfip)_4]_2$ salt is actually $Mg[B(hfip)_4]_2 \cdot 3DME$) are all potential contributors to decomposition during electrochemical oxidation, particularly when the voltage exceeds 3 V.[15] The side reactions caused by electrolyte decomposition can affect the charge-discharge performance of the electrode materials in multiple ways. A typical example is illustrated in **Figure 1(b)** and **1(c)**. In a 0.3 mol L^{-1}, $Mg[B(hfip)_4]_2$-G2 electrolyte containing 800 ppm H_2O, the Mg||MnO_2 cell exhibits a significantly higher capacity during the charging stage compared to the discharging stage. This leads to low coulombic efficiency and poor reversibility of the Mg||MnO_2 battery. Similar issues have been observed in our previous reports.[12a] This undoubtedly influences the development of Mg||TMOs batteries at the most fundamental level of material characterization. To identify the root cause of the issue, we begin our discussion with the current collector–electrolyte interface. For simplicity, the 0.3 mol L^{-1} $Mg[Al(hfip)_4]_2$-G2 and $Mg[B(hfip)_4]_2$-G2 electrolytes are hereafter referred to as AlHFIP electrolyte and BHFIP electrolyte, respectively. We selected Al foil with a graphite coating (abbreviated as Al@C) as the current collector, as it has been identified as one of the few options that exhibit resistance to corrosion in Mg||MnO_2 batteries and hold potential for practical application. Unless otherwise specified, the type of cell used in this study is as shown in **Figure S1**. This configuration ensures that only the investigated substrate participates in the electrochemical process. As shown in Figure 2, we first tested the performance of Mg||Al@C cells in the two electrolytes using the conventional cyclic voltammetry (CV) method. Multiple cycles are employed to minimize the influence of passivation on the Mg metal surface. The comparison between BHFIP with 800 ppm water and

AlHFIP with 200 ppm water was conducted because the electrochemical characteristics of the Mg metal anode in these two electrolyte systems are relatively consistent (can be found in **Figure S4**). This consistency helps to minimize misinterpretation of the cathode's electrochemical behavior that might arise from Mg passivation in water-containing electrolytes. As shown in **Figure 2(a)** and **2(b)**, in both AlHFIP electrolyte with 200 ppm H_2O and BHFIP electrolyte with 800 ppm H_2O, the response current caused by electrolyte decomposition at high voltage (> 4.5 V) decreases with each cycle. This indicates that electrolyte decomposition forms a film on the Al@C surface. However, the current at 4 V, shown in **Figure 2(c)**, reveals that the decomposition current during the first cycle is smallest in the BHFIP electrolyte with higher water content. This is because the overpotential on the Mg metal anode side is typically higher during the first cycle, making the initial data unrepresentative of the true characteristics of the electrolyte. This confirms the necessity of using multiple-cycle CV testing to assess the decomposition characteristics of electrolytes. Additionally, the current density values were taken from the reduction process, which minimizes misinterpretation of the decomposition voltage caused by polarization. The data in **Figure 2(c)** demonstrates that both electrolytes begin to decompose at 4 V. **Figure S2** and **Figure 2(d)** show that the appearance of Al@C remains nearly unchanged before and after testing. Similarly, **Figure 2(e)** and **2(f)** demonstrate that the structure of Al@C does not exhibit significant changes between pre- and post-testing. **Figure 2(g)** presents the electrochemical impedance spectroscopy (EIS) results of Al@C cells at different voltages. At 2.5 V and 3 V, the AlHFIP electrolyte (200 ppm H_2O) and the BHFIP electrolyte (800 ppm H_2O) display similar impedance characteristics. However, at voltages exceeding 3.5 V, the impedance associated with electrolyte decomposition in the AlHFIP electrolyte is smaller than that of the BHFIP electrolyte. This difference is more intuitively observed through the Distribution of Relaxation Times (DRT) analysis of EIS. As shown in **Figure 2(h_1)**, the possible charge transfer impedance values corresponding to AlHFIP at 3.5 V and 4 V are lower than those of the BHFIP electrolyte. This suggests that although the BHFIP

electrolyte contains a higher water content than the AlHFIP electrolyte, the BHFIP electrolyte exhibits better resistance to electrochemical oxidation. Interestingly, previous studies on the application of BHFIP and AlHFIP electrolytes in MRBs also emphasized their claimed resistance to moisture.[7a, 13]

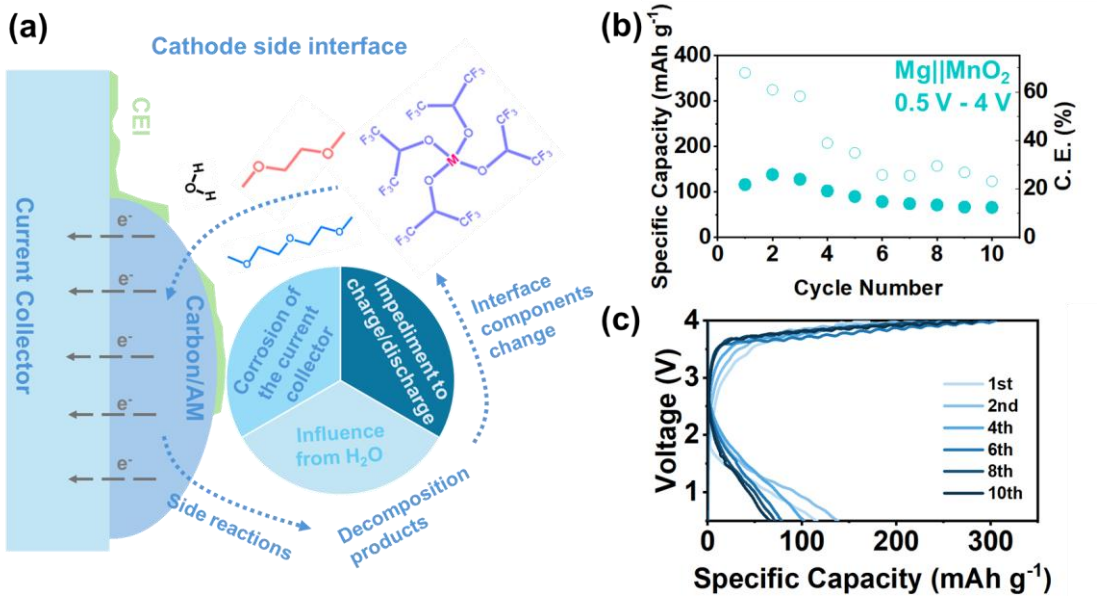

Figure 1. (a) Schematic illustration of the cathode-electrolyte interface in Mg batteries with ether-based electrolytes. (b) The charge-discharge performance of a Mg||MnO_2 cell as an example. The hollow circles correspond to the Coulombic efficiency. (c) The voltage profiles of the Mg||MnO_2 cell.

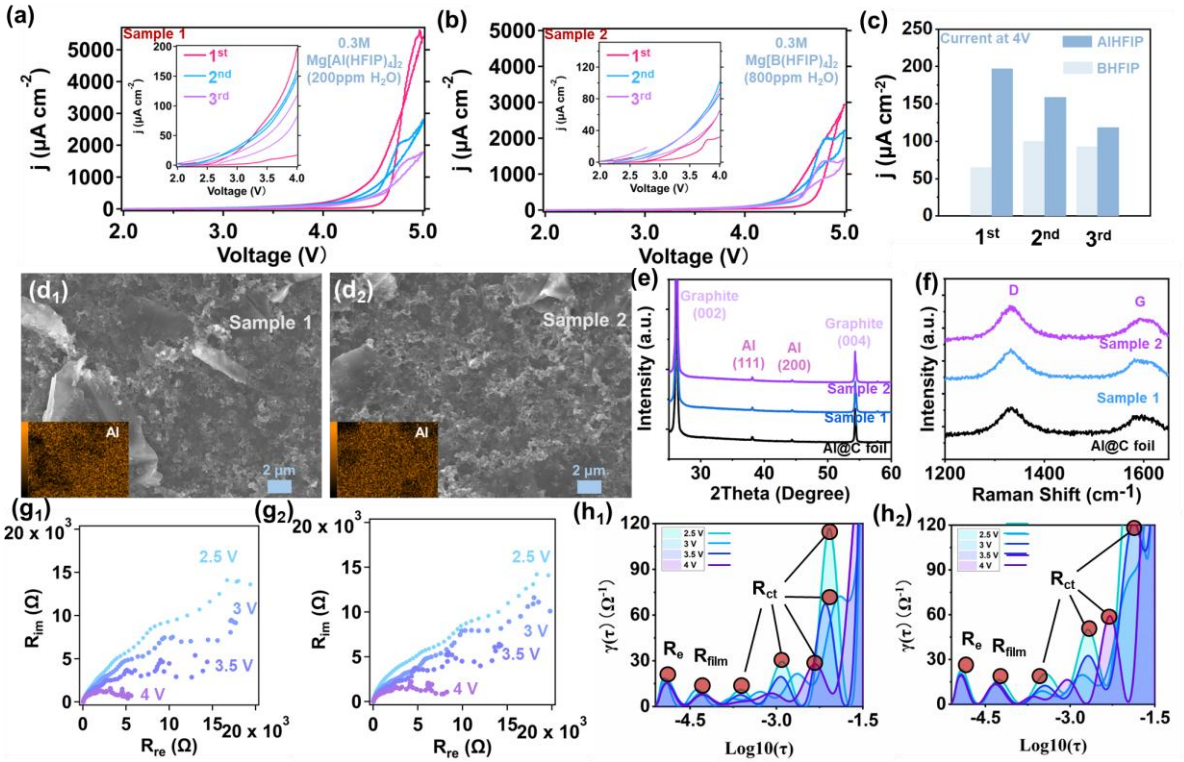

Figure 2. The electrochemical characteristics of Al@C foil in AlHFIP and BHFIP electrolytes. The CV curves of Al@C||Mg cells in (a) AlHFIP electrolyte (200 ppm H_2O content) and (b) BHFIP electrolyte (800 ppm H_2O content), with red, blue, and purple lines corresponding to the first, second, and third sweeps, respectively, at a sweep rate of 5 mV s^{-1}. The Al@C foils for testing are named Sample 1 and Sample 2. (c) Current densities at 4 V (reduction process) in different electrolytes during the CV tests. The 1^{st},2^{nd} and 3^{rd} refer to the number of sweep cycles. (d_1) (d_2) SEM and EDS images of Al@C after the CV tests. (e) XRD patterns and (f) Raman spectra of Al@C foil before and after the CV tests. Nyquist plots of Al@C foil in (g_1) the AlHFIP and (g_2) the BHFIP electrolytes at different voltages. (h_1)(h_2) DRT analysis results corresponding to the EIS tests.

Therefore, we further investigated the relationship between water content and the two electrolytes. By adding equal amounts of deionized water to AlHFIP (200 ppm H_2O content) and BHFIP (800 ppm H_2O content), we prepared four additional electrolytes, labeled BHFIP (0.46% H_2O content), BHFIP (1.34% H_2O content), AlHFIP (0.16% H_2O content), and AlHFIP (0.81% H_2O content). These four electrolytes are also tested in Mg||Al@C cells, with the results shown and summarized in **Figure 3(a)** and **Figure S3**. Apart from BHFIP (1.34% H_2O content),

which exhibited a higher decomposition current, the response currents at 4 V for the other three electrolytes decreased. This is attributed to the excessive water content causing passivation on the surface of the Mg metal, significantly increasing the overpotential for Mg deposition/dissolution. This observation is further confirmed by the data presented in **Figure S4** and **Figure S5**. At low water content, an increase in water content hinders the electrochemical reactions of Mg on the anode side while simultaneously suppressing electrochemical reactions on the cathode side (**Figure S6**). However, at high water content, the reactions in the cell partly transition to water electrolysis, leading to a rise in decomposition current. **Figure S7** illustrates the electrochemical characteristics of BHFIP electrolyte with only 200 ppm H_2O. For the BHFIP electrolyte containing 200 ppm water, the current at 3.2 V for the 1st, 2nd, and 3rd cycles was 3.75, 6.90, and 3.75 μA cm^{-2}, respectively; at 4.0 V, the corresponding current density were 38.26, 45.01, and 26.07 μA cm^{-2}, respectively. This performance is markedly better than that observed for the BHFIP electrolyte containing 800 ppm water, the latter one exhibited current density of 65.2, 100, and 92.8 μA cm^{-2} for the first three cycles at 4.0 V. It is evident that, when both electrolytes have the same water content, BHFIP exhibits stronger oxidative resistance compared to AlHFIP. However, increasing the water content within a certain range still makes BHFIP electrolytes more prone to decomposition. This finding indicates that in both AlHFIP and BHFIP electrolytes, trace amounts of water molecules participate in electrochemical processes at both the cathode and anode sides. Therefore, neither electrolyte demonstrates a truly moisture-resistant capability in a strict sense. Another noteworthy issue is that the final water content of AlHFIP and BHFIP electrolytes was not identical, after adding the same amount of water. To explain this, we performed Fourier transform infrared spectroscopy (FT-IR) analysis on the two electrolytes with varying water content, as exhibited in Figure 3b. As depicted in **Figures 3(b_1)** and **Figures 3(b_2)**, with the increase in water content in the BHFIP electrolyte, the peaks corresponding to O-H vibrations became significantly stronger. At the same time, the peaks associated with the

organic solvent showed slight weakening and a blue shift, which can be attributed to the dilution effect of G2. BHFIP electrolyte, on the other hand, is less likely to undergo this process. This leads to distinct responses when water enters the electrolytes. For BHFIP electrolyte, water molecules are incorporated into the electrolyte and may coordinate Mg ions. In contrast, $[Al(hfip)_4]^-$ counteracts the entry of small amounts of water molecules through a self-sacrificial mechanism involving its anions, which might explain the misconception in other reports that AlHFIP electrolytes are moisture-resistant. By directly adding deionized water to the two electrolyte systems, distinct differences in appearance can be rapidly observed. As shown in **Figure 3(c)**, when varying amounts of water were added to 0.5 mL of electrolyte, the BHFIP electrolyte exhibited only slight turbidity after the addition of 10 μL of water, whereas the appearance of AlHFIP changed to a gel-like state upon the addition of 10 μL of water. Considering that the only difference between the two electrolytes is the type of anion, this result stems from the interaction between the anion in AlHFIP and water. The primary distinction between the anions in the AlHFIP and BHFIP electrolytes lies in their central atoms: Al^{3+} is a stronger Lewis acid than B^{3+}, rendering it more susceptible to interaction with water molecules. Moreover, the Al–O bond is weaker than the B–O bond, making Al-centered anions more sensitive to moisture. Given that AlHFIP is not stable in the presence of water, we focused on BHFIP electrolyte and conducted in-situ Raman spectroscopy to study its decomposition on electrode surfaces. As shown in **Figure 3(d)**, when the voltage increases beyond 3 V, non-free-state anions and associated solvent molecules are oxidized at the electrode surface. During this process, a small number of water molecules may decompose:

$$H_2O \rightarrow 2H^+ + 1/2\ O_2 + 2e^- \quad \text{(Equation 1)}$$

The resulting protons could act as catalysts to accelerate the oxidative decomposition of the electrolyte, potentially representing a key mechanism by which moisture affects BHFIP electrolytes. However, due to the low water content of the available electrolytes, we were unable to directly identify the role of water molecules in interfacial electrochemical processes.

To address this, we used Molecular Dynamics (MD) simulations to model the possible ionic configurations in water-containing electrolytes.

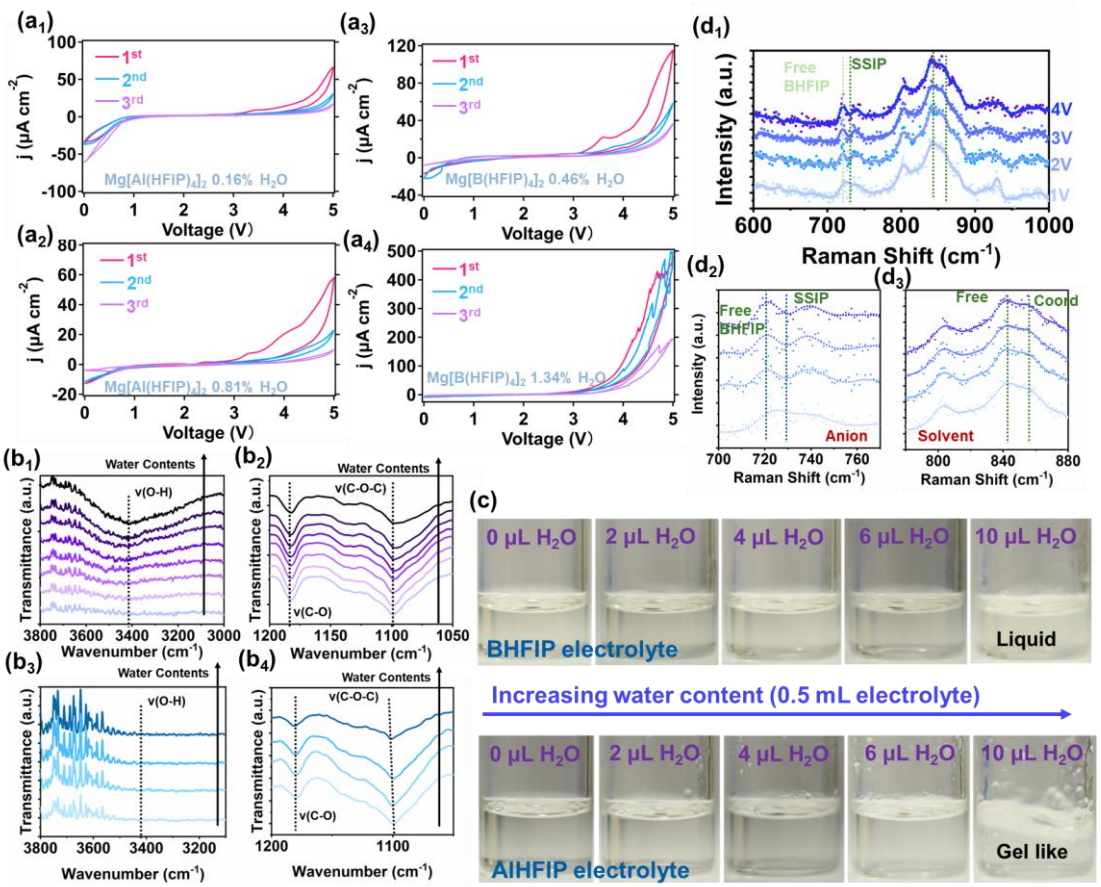

Figure 3. The electrochemical characteristics of Al@C foil in AlHFIP and BHFIP electrolytes with different H_2O contents. The CV curves of Al@C||Mg cells in (a_1) AlHFIP electrolyte (0.16% H_2O content), (a_2) AlHFIP electrolyte (0.81% H_2O content), (a_3) BHFIP electrolyte (0.46% H_2O content) and (a4) BHFIP electrolyte (1.34% H_2O content) at a sweep rate of 5 mV s^{-1}. FTIR spectra of (b_1) and (b_2) BHFIP electrolyte and (b_3) and (b_4) AlHFIP electrolyte with increasing water content from bottom to top. (c) Appearance changes of BHFIP electrolyte (top) and AlHFIP electrolyte (bottom) upon the addition of water. (d_1) (d_2) (d_3) In-situ Raman spectra of the Al@C foil surface at different voltages in BHFIP electrolyte with 800 ppm water content.

The simulation results of BHFIP electrolytes obtained via the MD method are shown in **Figure 4(a)**. As the water content increases, H_2O gradually replaces G2 in the inner solvation shell structure. This can also be observed in **Figure 4(b)**, where the coordination number of G2

around Mg^{2+} decreases from 2 at low water content (0.1%) to less than 2 at high water content (10%). This occurs because H_2O has a higher solvation energy for Mg compared to G2, meaning that the hydrated structure of Mg^{2+} is more stable. Correspondingly, the coordination number of water molecules gradually increases with the addition of water (**Figure S8**), also confirming this perspective. The DFT calculation results shown in **Figure 4(d)** and **Figure S9** support this observation. The binding energies for the formation of different solvation structures of Mg^{2+} follow the order $Mg(H_2O)_6^{2+} > Mg(DME)_3^{2+} > Mg(H_2O)_3(G2)^{2+} > Mg(G2)_2^{2+}$. This indicates that water molecules can replace G2 or DME to form more stable solvation structures with Mg^{2+}. Among these, water molecules typically exhibit higher charge density, giving them greater potential to participate in electrochemical reactions. Due to the relatively low concentration of DME, even though the solvation energies of DME and G2 are comparable, the vast majority of DME molecules exist in an uncoordinated (free) status (**Figure S10**). The in-situ Raman spectra in **Figure 4(c)** confirm this solvation structure transition as more water is added to the BHFIP electrolyte. As the water content increases, the proportion of free G2 molecules in the electrolyte also rises. For the AlHFIP electrolyte, however, the addition of water leads to gelation of the electrolyte, and the solvent peaks show a trend opposite to that of BHFIP (**Figure S11**). The Raman spectra of anions in BHFIP electrolytes with different water contents are also provided in **Figure S12**, which supports our idea. Furthermore, the results obtained from MD simulations using different force fields (universal force field, UFF) have been included in **Figure S13** to provide additional reference information. It can be observed that the trend of the impact of water molecules on the electrolyte structure remains unchanged regardless of the force field employed. **Figure S14** depicts the electric double-layer (EDL) structure and electric double-layer capacitance (EDLC) characteristics for electrolytes with varying water content. It confirms that water molecules penetrate the cathode–electrolyte interface and cause the EDL thickness at the electrode surface decreases, thereby rendering desolvation increasingly difficult. At this point, we can summarize a possible schematic of the

electrode/electrolyte interface in BHFIP electrolytes, as shown in **Figure 4(e)**. In electrolytes containing a small amount of water, the higher solvation energy of H_2O molecules makes it more challenging for hydrated Mg ions to undergo complete desolvation. Consequently, partially hydrated Mg ions remain on the electrode surface and participate in electrode reactions, whether at the cathode or anode.

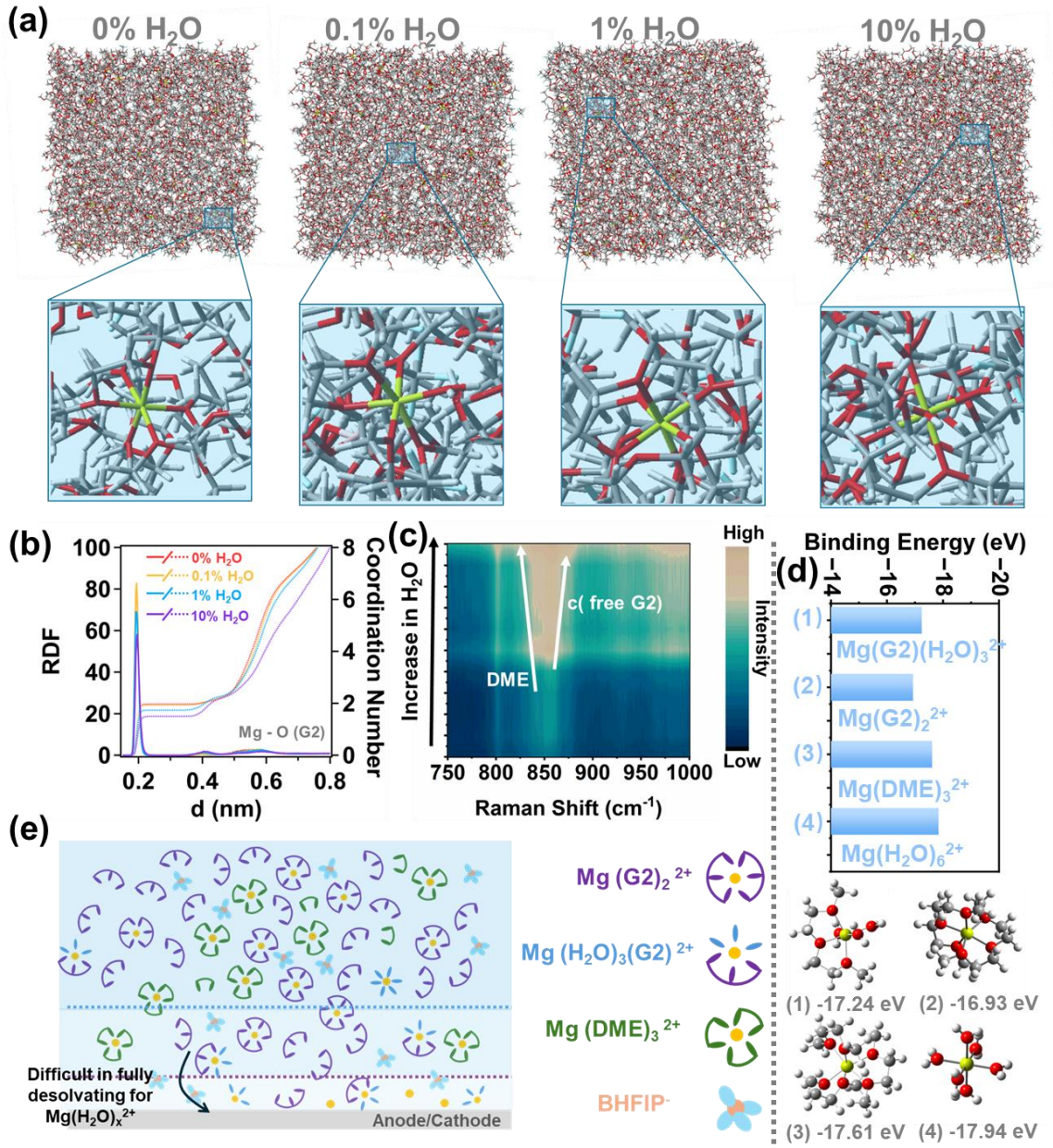

Figure 4. (a) MD simulations of BHFIP electrolyte with varying water contents. From left to right: 0%H_2O, 0.1% H_2O, 1% H_2O, and 10% H_2O. (b) RDF and G2 coordination number analysis of Mg-ion corresponding to figure (a). (c) In-situ Raman spectra of BHFIP electrolytes with the addition of H_2O, along with (d) Mg-ion solvation structures and solvation energy. (e)

Schematic illustration of the electrode-electrolyte interface in water-containing BHFIP electrolytes.

Considering that water content influences the decomposition behavior of electrolytes on the cathode surface, we further analyzed the composition left on the Al@C electrode surface after electrolyte decomposition for different electrolytes. As shown in Figure 5, BHFIP electrolytes (800 ppm H_2O content) and BHFIP electrolytes (0.46% H_2O content) were used to assemble Mg||Al@C cells, followed by the constant voltage tests illustrated in **Figure 5(c)**. After testing, the Al@C foil was carefully rinsed several times with DME in a glovebox to remove residual electrolyte and then transferred to X-ray photoelectron spectroscopy (XPS) analysis under non-exposed conditions. As shown in **Figure 5(a)**, for the BHFIP electrolyte with lower water content (800 ppm), the surface composition includes residual BHFIP anions that could not be entirely washed away and a small amount of decomposition products. This layer is very thin, with a thickness of ≤1.5 nm. Furthermore, **Figure S15**, **Figure S16** and **Figure 5(a_3)** reveals the presence of decomposition products derived from the solvent on the electrode surface. This indicates that for electrolytes with lower water content, the cathode-electrolyte interface (CEI) is relatively thin and primarily consists of organic components formed by solvent decomposition. **Figure 5(b)** shows that at higher water content, the decomposition of anions becomes more significant, leading to a notable increase in both the fluorine-containing components and the thickness of the CEI. This confirms that the presence of water promotes the decomposition of the BHFIP electrolyte. Considering that the detection depth of XPS typically spans several nanometers, the persistent graphite peak in **Figure 5(b_3)** indicates that the CEI formed is likely porous and unevenly distributed. This explains why the current from electrolyte decomposition reactions decreases over repeated CV testing but does not disappear entirely. It also suggests that in BHFIP electrolytes, it is challenging to form a CEI on the cathode side that can effectively prevent side reactions. The current density observed in **Figure**

5(c) shows slight differences compared to that in the CV tests. This is likely due to differences in the state of the Mg anode and inherent variations between electrochemical sweeping tests and constant voltage tests. In this electrolyte, the Mg anode is sufficient to sustain low-current, continuous side reactions. Gas chromatography (GC) tests on the same cells confirm that oxygen generation occurs in water-containing BHFIP electrolytes, supporting the notion that reactions at both the cathode and anode partially transition to water splitting at higher water content (**Figure S17**). Based on these findings, we can infer the behavior at the cathode-electrolyte interface in BHFIP electrolytes. As illustrated in **Figure 5(d)**, on the surface of Al@C, the decomposition of solvent and water under high voltage generates oxygen gas and a small number of protons at the cathode surface. In the absence of active materials, the protons catalyze the decomposition of electrolyte components at the electrode surface, leading to the formation of a thicker but uneven CEI. This CEI cannot effectively prevent the continuous consumption of the BHFIP electrolyte and may even accelerate localized reactions, leading to a more unstable electrode-electrolyte interface.

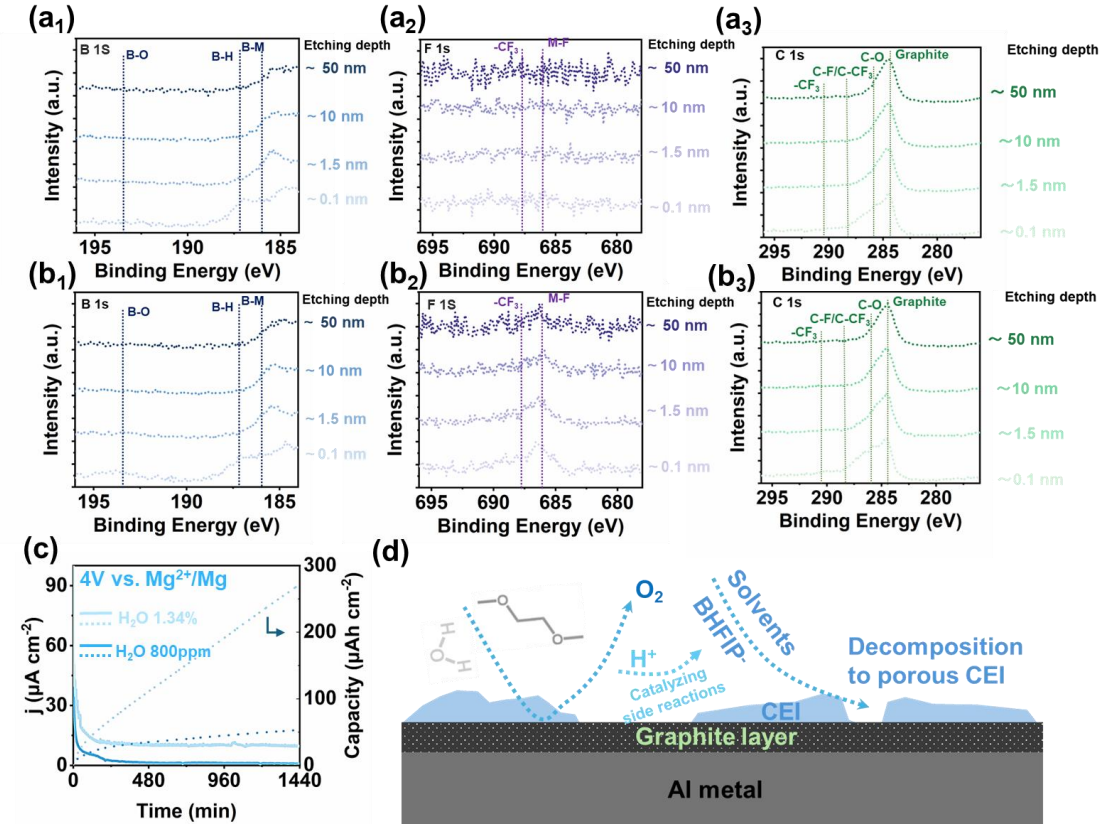

Figure 5. XPS depth profiles used to analyze the decomposition of BHFIP electrolyte on the surface of Al@C foil. Surface composition analysis of Al@C in Al@C||Mg cells after constant voltage testing with BHFIP electrolytes containing (a_1) (a_2) (a_3) 800 ppm water and (b_1)(b_2)(b_3) 1.34% water. (c) Current-time curves during the 4 V constant voltage test. (d) Proposed decomposition mechanism of water-containing BHFIP electrolytes on the cathode surface under high voltage conditions.

We also conducted a similar analysis for the AlHFIP electrolyte, as shown in **Figure S18**, where we confirmed that water also promotes the decomposition of AlHFIP electrolytes. However, unlike the BHFIP electrolyte, the electrode surface influenced by water-containing AlHFIP electrolytes contains more inorganic components, such as aluminum hydroxides, formed as a result of reactions with water. Additionally, the spontaneous reaction between the electrolyte and water reduces the generation of oxygen at the electrode surface. These findings are further supported by the data presented in **Figure S19** – **Figure S21**. Before analyzing the discharge characteristics of TMOs electrodes in different electrolytes, the influence of conductive porous carbon was also evaluated. **Figure S22**–**Figure S25** present a detailed analysis of the behavior of three commonly used conductive porous carbons—Super P (SP), Ketjen Black (KB), and Acetylene Black (AB)—in various electrolytes.

As shown in **Figure S22** and **S23**, the use of KB as conductive carbon resulted in the most severe side reactions, indicating a direct relationship between the electrode's specific surface area and electrolyte decomposition. Electrodes with larger surface areas tend to cause more severe electrolyte decomposition. **Figure S24** and **Figure S25** further demonstrate that the decomposition behavior of the electrolyte on electrodes coated with conductive porous carbon is consistent with that on original Al@C foil. This suggests that the presence of porous carbon provides additional reaction sites through its pores but does not catalyze the decomposition reactions themselves. Based on this, AB, which resulted in the smallest side reaction current, was selected as the conductive material for electrode preparation. Another important point to

note is that stainless steel is not a suitable current collector for both BHFIP and AlHFIP electrolytes. **Figure S26** and **Figure S27** reveal significant corrosion of stainless steel in these electrolytes. This is why Swagelok cells were chosen for testing: coin cells are not a suitable choice for these WCA-based ether electrolytes.

Finally, we return to the initial question: why do TMOs electrodes exhibit poor coulombic efficiency and reversibility in these WCA-based electrolytes? In Figure 6, we assembled Mg||MnO_2 cells using four types of electrolytes and conducted constant current charge-discharge tests in the voltage range of 0.5–4 V. It is important to note that, unlike earlier sections, the "BHFIP electrolyte (0.5% water content)" here refers to BHFIP electrolyte with 200 ppm water content to which 0.5% volume of DI-water was added, and the same applies to the AlHFIP electrolyte. As shown in **Figure 6(a)** and **Figure 6(b)**, the charging capacity of the cell using BHFIP electrolyte (0.5% water content) is significantly higher than that of the other cells, while the discharging capacity is similar to the others. This indicates that the side reactions induced by the decomposition of water-containing electrolytes are the main source of the irreversible capacity. From the third cycle, the discharging capacity exhibits a trend in increasing that is similar to the charging capacity. This could be attributed to the protons generated by the side reactions, which may promote the dissolution of MnO_2 at high voltages. This facilitates a more reversible conversion reaction of Mn-ions on the cathode surface. However, the Mn^{2+} ions entering the electrolyte can shuttle to the anode side, where they deposit, making this portion of reversible capacity unsustainable in the long-term charge-discharge cycle.[16] For the AlHFIP electrolyte (0.5% water content), although the cell still exhibit a charging capacity higher than the discharging capacity, the difference between the two is significantly smaller compared to the BHFIP electrolyte (0.5% water content). This is attributed to the self-sacrificial moisture resistance characteristic of the AlHFIP electrolyte. However, as a trade-off, the poorer ionic conductivity and passivation of the Mg anode, resulting in the lowest discharging capacity among the tested cells (**Figure 6(c)**). For the AlHFIP electrolyte

(200 ppm water content), the corresponding cell exhibited more severe side reactions at high voltages, consistent with our previous conclusion. In contrast, the cell with the BHFIP electrolyte (200 ppm H_2O content) demonstrated the best reversibility, indicating that BHFIP electrolyte, when the water content does not exceed 200 ppm, has the potential to support Mg||TMOs batteries operating stably within a wide voltage window.

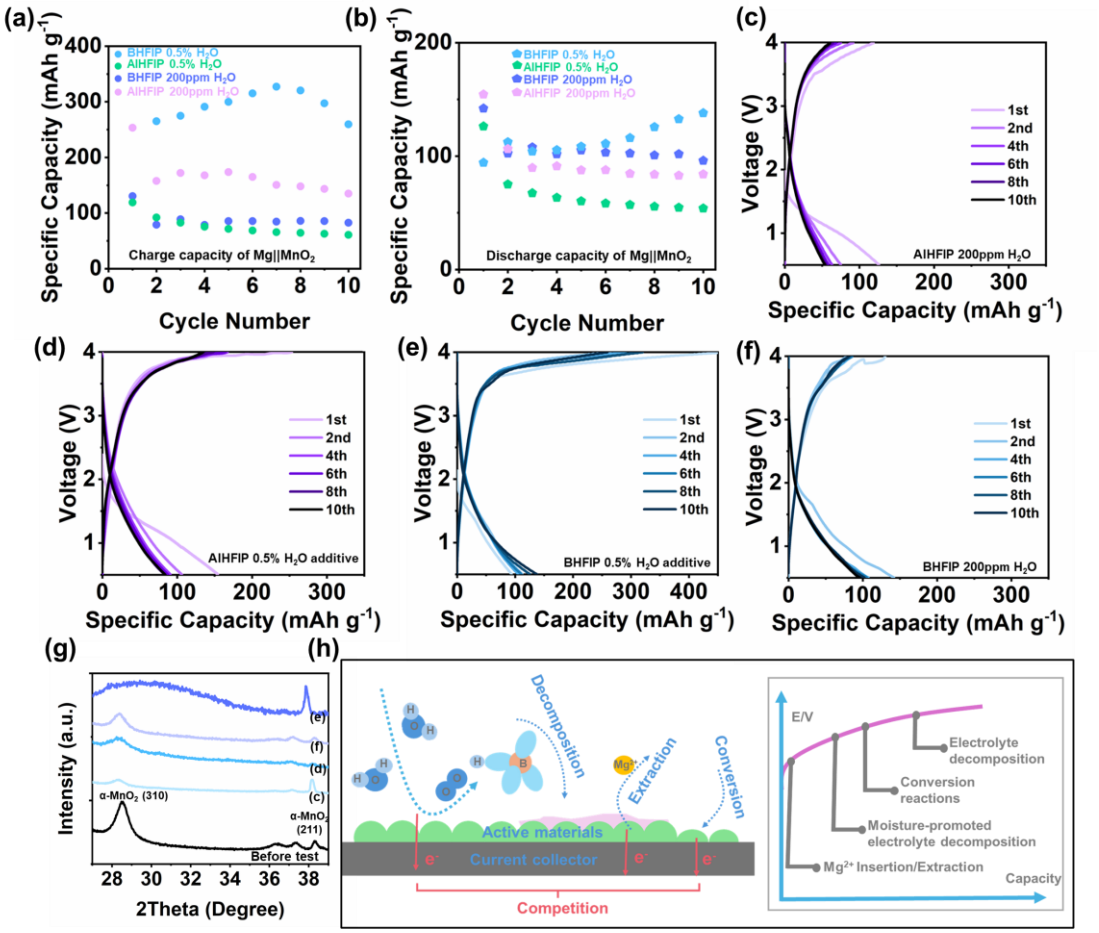

Figure 6. Performance of Mg||MnO_2 cells using electrolytes with equal amounts of added water. (a) Capacity of charging and (b) discharging of Mg||MnO_2 cells. Voltage profiles of the cell with (c) AlHFIP electrolyte with 200 ppm water content, (d) AlHFIP with 0.5% added water (volume ratio), (e) BHFIP with 0.5% added water, and (f) BHFIP with 200 ppm water content. (g) XRD patterns of the MnO_2 electrodes after cycling. (h) Schematic illustration of the cathode-electrolyte interface at high voltage for TMO cathodes.

The XRD patterns of MnO_2 before and after testing are shown in **Figure 6(g)**, with image labels corresponding to their respective samples. The α-MnO_2 electrode in the BHFIP electrolyte

(0.5% H_2O content) displayed a transformation of the (310) peak into a broad peak, suggesting that a significant portion of α-MnO_2 was converted into nanocrystals or amorphous structures via a possible dissolution mechanism that can be promoted by the presence of proton:

$Mg^{2+} + 2MnO_2 + 2e^- \rightarrow 2Mg_{0.5}MnO_2$ (Equation 2)

$2Mg_{0.5}MnO_2 \rightarrow MgO + Mn_2O_3$ (Equation 3)

$MgO + 2H^+ \rightarrow Mg^{2+} + H_2O$ (Equation 4)

Or the direct dissolution of TMOs cathodes:

$MnO_2 + 4H^+ + 2e^- \rightarrow Mn^{2+} + 2H_2O$ (Equation 5)

The regenerated H_2O explains the phenomenon where TMO-based cathodes can enhance electrolyte decomposition: H_2O acts as a catalyst in some side reactions. For the MnO_2 electrodes in the other electrolytes, the (310) peak showed a slight shift to lower angles, indicating minor Mg^{2+} insertion into the material, while the crystalline structure remained largely intact. The charge-discharge curves further reveal that due to the poor kinetics of Mg^{2+} insertion and de-insertion reactions, the electrode reactions are predominantly limited to the surface. As a result, the charge-discharge profiles exhibit pronounced pseudocapacitive characteristics. **Figure S28**–**Figure S30** provide additional details on the morphological and compositional changes of the electrodes before and after cycling. The morphology of the α-MnO_2 nanowires remained relatively intact after cycling, but the elemental composition showed increased Mg content, consistent with the XRD results. This indicates that, under ambient conditions and with limited side reactions, the reversibility of Mg||MnO_2 batteries is primarily due to cathode reactions occurring almost exclusively on the surface of the active material.

For the BHFIP electrolyte (200 ppm H_2O content), the Mg||MnO_2 battery maintained a reversible capacity of 70.6 mAh g^{-1} after 50 cycles, with a coulombic efficiency of approximately 96.7% during cycles 40–50 (**Figure S31**). At this point, we can more comprehensively speculate on the possible changes occurring at the electrode interface in these WCA-based ether electrolytes containing small amounts of water, as illustrated in **Figure 6(h)**.

Taking the BHFIP electrolyte as an example, the decomposition of trace water at the cathode surface typically begins at low voltages. The resulting protons catalyze further decomposition of the electrolyte at the electrode surface while also accelerating the degradation of active materials. Due to the formation of the porous CEI, which fails to effectively prevent side reactions, the Mg^{2+} insertion and extraction reactions are forced to compete with these ongoing side reactions. However, if the water content in the electrolyte can be effectively minimized, BHFIP electrolytes could potentially support the charge and discharge of electrode materials under conditions not exceeding 4 V. This presents a promising pathway for the development of high-energy-density Mg||TMOs batteries.

3. Conclusion

In summary, through the study of the electrochemical behavior of BHFIP and AlHFIP electrolytes with varying water content on Al@C current collectors and MnO_2 cathodes, we have identified the characteristics of these two representative WCA-based ether electrolytes. We have clarified the sources of their differences and corrected some misconceptions from previous studies about this class of electrolytes. We confirmed that AlHFIP and BHFIP electrolytes exhibit different behaviors upon the introduction of water molecules, with water promoting electrolyte decomposition on the cathode side and damaging the active material. Among the two, BHFIP electrolyte demonstrated better stability. By reducing the water content in the electrolyte, BHFIP electrolyte is able to support highly reversible cycling of Mg||MnO_2 batteries for 50 cycles. This highlights the importance of monitoring the water content in such electrolytes during use. Additionally, it suggests that in MRBs development, designing materials and electrodes capable of mitigating the impact of water could significantly enhance battery performance.

Supporting Information

Supporting Information is available from the Wiley Online Library or from the author.

Acknowledgements

This work was supported by JSPS KAKENHI (23K13816) and JST GteX (JPMJGX23S1). A part of this work was conducted at the Laboratory of XPS analysis, Joint-use facilities, Hokkaido University. We thank Laboratory of Interfacial Electrochemistry (Hokkaido University) for helping with the GC test; Physical Chemistry Lab (Hokkaido University) for helping with the Raman measurement.

Received: ((will be filled in by the editorial staff))
Revised: ((will be filled in by the editorial staff))
Published online: ((will be filled in by the editorial staff))

References

[1] a) X.-G. Yang, T. Liu, S. Ge, E. Rountree, C.-Y. Wang, *Joule* **2021**, 5, 1644; b) M. Dixit, A. Bisht, R. Essehli, R. Amin, C. M. Kweon, I. Belharouak, *ACS Energy Lett.* **2024**, 9, 934; c) S. Guo, Y. Wang, L. Dai, H. Hu, *eTransportation* **2023**, 17, 100251.

[2] a) J. W. Choi, D. Aurbach, *Nature Reviews Materials* **2016**, 1; b) F. Liu, G. Cao, J. Ban, H. Lei, Y. Zhang, G. Shao, A. Zhou, L. Z. Fan, J. Hu, *Journal of Magnesium and Alloys* **2022**, 10, 2699; c) C. Wei, L. Tan, Y. Zhang, Z. Wang, J. Feng, Y. Qian, *Energy Storage Materials* **2022**, 52, 299.

[3] a) Z. Lu, A. Schechter, M. Moshkovich, D. Aurbach, *Journal of Electroanalytical Chemistry* **1999**, 466, 203; b) D. Aurbach, Z. Lu, A. Schechter, Y. Gofer, H. Gizbar, R. Turgeman, Y. Cohen, M. Moshkovich, E. Levi, *Nature* **2000**, 407, 724.

[4] a) D. Aurbach, G. S. Suresh, E. Levi, A. Mitelman, O. Mizrahi, O. Chusid, M. Brunelli, *Advanced Materials* **2007**, 19, 4260; b) O. Mizrahi, N. Amir, E. Pollak, O. Chusid, V. Marks, H. Gottlieb, L. Larush, E. Zinigrad, D. Aurbach, *Journal of The Electrochemical Society* 2008, 155, A103.

[5] a)L. Yang, C. Yang, Y. Chen, Z. Pu, Z. Zhang, Y. Jie, X. Zheng, Y. Xiao, S. Jiao, Q. Li, D. Xu, *ACS Appl. Mater. Interfaces* **2021**, 13, 30712; b) Y. He, Q. Li, L. Yang, C. Yang, D. Xu, *Angew. Chem. Int. Ed.* **2019**, 58, 7615; c) T. Gao, S. Hou, F. Wang, Z. Ma, X. Li, K. Xu, C. Wang, *Angew. Chem. Int. Ed.* **2017**, 56, 13526; d) S. Fan, G. M. Asselin, B. Pan, H. Wang, Y. Ren, J. T. Vaughey, N. Sa, *ACS Appl. Mater. Interfaces* **2020**, 12, 10252.

[6] a) K.-C. Lau, T. J. Seguin, E. V. Carino, N. T. Hahn, J. G. Connell, B. J. Ingram, K. A. Persson, K. R. Zavadil, C. Liao, *Journal of The Electrochemical Society* **2019**, 166, A1510; b) H. Dong, O. Tutusaus, Y. Liang, Y. Zhang, Z. Lebens-Higgins, W. Yang, R. Mohtadi, Y. Yao, *Nature Energy* **2020**, 5, 1043; c)A. Schmidt, H. Koger, A. Barthélemy, G. Studer, B. Esser, I. Krossing, *Batteries & Supercaps* **2022**, 5, e202200340

[7] a) Z. Zhao-Karger, M. E. Gil Bardaji, O. Fuhr, M. Fichtner, Journal of Materials Chemistry A 2017, 5, 10815; b) B. Dlugatch, M. Mohankumar, R. Attias, B. M. Krishna, Y. Elias, Y. Gofer, D. Zitoun, D. Aurbach, *ACS Appl. Mater. Interfaces* **2021**, 13, 54894.

[8] J. Zhu, Y. Guo, J. Yang, Y. Nuli, F. Zhang, J. Wang, S.-i. Hirano, *Journal of Power Sources* **2014**, 248, 690.

[9] a) R. Zhang, X. Yu, K.-W. Nam, C. Ling, T. S. Arthur, W. Song, A. M. Knapp, S. N. Ehrlich, X.-Q. Yang, M. Matsui, *Electrochemistry Communications* **2012**, 23, 110; b) X. Ye, K. Shimokawa, Y. Kezuka, T. Hatakeyama, H. Li, T. Ichitsubo, *The Journal of Physical Chemistry C* 2023, 127, 5210; c) R. Trocoli, P. Parajuli, C. Frontera, A. P. Black, G. C. B. Alexander, I. Roy, M. E. Arroyo-de Dompablo, R. F. Klie, J. Cabana, M. R. Palacin, *ACS Appl. Energy Mater.* 2022, 5, 11964.

[10] a) X. Sun, V. Duffort, B. L. Mehdi, N. D. Browning, L. F. Nazar, *Chemistry of Materials* **2016**, 28, 534; b) M. Mao, T. Gao, S. Hou, C. Wang, *Chem. Soc. Rev.* **2018**, 47, 8804.

[11] R. Iimura, S. Kawasaki, T. Yabu, S. Tachibana, K. Yamaguchi, T. Mandai, K. Kisu, N. Kitamura, Z. Zhao-Karger, S. I. Orimo, Y. Idemoto, M. Matsui, M. Fichtner, I. Honma, T. Ichitsubo, H. Kobayashi, *Small* **2025**, e2411493.

[12] a) H. Kobayashi, Y. Fukumi, H. Watanabe, R. Iimura, N. Nishimura, T. Mandai, Y. Tominaga, M. Nakayama, T. Ichitsubo, I. Honma, H. Imai, ACS Nano 2023, 17, 3135; b)R. Iimura, H. Watanabe, T. Mandai, I. Honma, H. Imai, H. Kobayashi, *ACS Applied Energy Materials* **2024**, 7, 5308.

[13] T. Pavcnik, M. Lozinsek, K. Pirnat, A. Vizintin, T. Mandai, D. Aurbach, R. Dominko, J. Bitenc, *ACS Appl. Mater. Interfaces* **2022**, 14, 26766.

[14] a) Z. Li, O. Fuhr, M. Fichtner, Z. Zhao-Karger, *Energy & Environmental Science* **2019**, 12, 3496-3501. b) J. Li, H. Fu, M. Gu, J. Chen, J. Zhou, L. Fan, B. Lu, *Nano Lett.* **2024**, *24*, 11419-11428. c) B. Gui, X. Yang, H. Fu, P. Peng, W. Lyu, A. M. Rao, J. Zhou, L. Fan, B. Lu, *Angew. Chem. Int. Ed.* **2025**, *64*, e202421928..

[15] X. Ren, L. Zou, X. Cao, M. H. Engelhard, W. Liu, S. D. Burton, H. Lee, C. Niu, B. E. Matthews, Z. Zhu, C. Wang, B. W. Arey, J. Xiao, J. Liu, J.-G. Zhang, W. Xu, *Joule* **2019**, 3, 1662.

[16] X. Ye, H. Li, T. Hatakeyama, H. Kobayashi, T. Mandai, N. L. Okamoto, T. Ichitsubo, *ACS Appl. Mater. Interfaces* **2022**, 14, 56685.